ADVANCED FUNCTIONAL MATERIALS
www.afm-journal.de

New Understanding and Improvement in Sintering Behavior of Cerium-Rich Perovskite-Type Protonic Electrolytes

*Zehua Wang, Zhixin Luo, Hengyue Xu, Tianjiu Zhu, Daqin Guan, Zezhou Lin, Ting-Shan Chan, Yu-Cheng Huang, Zhiwei Hu, San Ping Jiang, and Zongping Shao**

Protonic ceramic cells show great promises for electrochemical energy conversion and storage, while one of the key challenges lies in fabricating dense electrolytes. Generally, the poor sinterability of most protonic ceramic electrolytes, such as $BaZr_{0.1}Ce_{0.7}Y_{0.1}Yb_{0.1}O_{3-\delta}$, is attributed to the Ba evaporation at high temperatures. In a systematic and comparative study of $BaCeO_3$ and $BaZrO_3$, the results demonstrated that Ba tends to segregate to grain boundaries rather than evaporate. Additionally, thermal reduction of Ce^{4+} to Ce^{3+} promotes the displacement of Ce to the Ba-site or the exsolution of CeO_2 phase, leading to an abnormal lattice shrinkage of perovskite phase and hindering the electrolyte densification. Contrary to previous beliefs that Ba deficiency inhibits the electrolyte sintering, the findings indicate that it surprisingly promotes the sintering of $BaZrO_3$ perovskites, while excess Ba negatively affects its sintering behavior due to the accumulation of Ba species at grain boundaries. As to $BaCeO_3$, excess Ba improves electrolyte sintering by suppressing the Ce exsolution at high temperatures. Meanwhile, Co-doping Zr and Ce in the B-site of protonic perovskite can optimize the sintering characteristic. These findings offer new insights into sintering of protonic perovskites and provide guidance for the development of new protonic devices.

1. Introduction

In light of the urgent need to achieve carbon neutrality and promote sustainable societal development, electrochemical energy conversion and storage devices have attracted considerable attention over the past few decades, stemmed from their ability to effectively bridge the gap between renewable energies and existing, well-established energy infrastructures.[1] Among them, solid oxide fuel cells (SOFCs) and electrolysis cells (SOECs) hold particular promise due to their high reaction kinetics, fuel flexibility, high round-trip efficiency, and cost-effectiveness in terms of materials.[2] However, the commercialization of conventional SOFCs and SOECs, which rely on oxygen-ion conducting electrolytes, still faces substantial challenges owing to the high operation temperature, such as performance degradation, high operational costs, and low reliability.[3] Consequently, significant efforts have been dedicated to improving cell durability and simplifying management systems by reducing the operating temperatures to intermediate ranges (400–600 °C).[4] Considering the greater proton mobility compares to that of oxygen-ions, protonic ceramic cells (PCCs) hold a greater promise for lower temperature operation.[5] Therefore, there has been an increasing interest in PCCs for electrochemical energy conversion and storage in recent times.

For both oxygen-ion and proton-conducting electrolytes-based cells, a prerequisite is that the electrolytes should be fabricated

Z. Wang, Z. Luo, T. Zhu, D. Guan, Z. Lin, S. P. Jiang, Z. Shao
WA School of Mines: Minerals
Energy and Chemical Engineering (WASM-MECE)
Curtin University
Perth, WA 6102, Australia
E-mail: zongping.shao@curtin.edu.au

H. Xu
Tsinghua Shenzhen International Graduate School
Tsinghua University
Shenzhen 518055, China

The ORCID identification number(s) for the author(s) of this article can be found under https://doi.org/10.1002/adfm.202402716

DOI: 10.1002/adfm.202402716

T. Zhu
School of Chemical Engineering
The University of Queensland
Brisbane 4072, Australia

Z. Lin
Department of Applied Physics and Research Institute for Smart Energy
The Hong Kong Polytechnic University
Hong Kong 999077, China

T.-S. Chan, Y.-C. Huang
National Synchrotron Radiation Research Center
101 Hsin-Ann Road, Hsinchu 30076, Taiwan

Z. Hu
Max-Planck-Institute for Chemical Physics of Solids
Nöthnitzer Str. 40, 01187 Dresden, Germany

S. P. Jiang
Foshan Xianhu Laboratory of the Advanced Energy Science and Technology Guangdong Laboratory
Foshan 528216, China

into dense membranes to avoid direct physical contact between the fuel gas and oxidant (O_2), thereby maximizing the cell thermodynamic efficiency and providing sufficient mechanical strength. Currently, most of the protonic perovskite electrolytes were developed by doping the parent oxides of $BaCeO_3$ (BCO) and $BaZrO_3$ (BZO). In particular, the formation of solid solution between BCO and BZO delivers an effective trade-off between chemical stability and ionic conductivity.[6] Owing to their high refractoriness, the sintering temperature of BZO-based electrolytes usually exceeds 1400 °C. However, segregated particles and pores were still detected on the electrolyte surface after sintering at 1700 °C, which has been attributed to the Ba volatilization at high temperatures.[7] Therefore, strategies to improve the sinterability of these materials have focused on mitigating the Ba loss by controlling the chemical stoichiometry of Ba and adjusting the sintering atmosphere.[8] Interestingly, recent studies also reported that Ba deficiency can facilitate the densification of Ba-based perovskites, which is ascribed to the enhanced diffusion rate of A-site cations.[8b,9] These findings suggest that factors other than Ba evaporation may also influence the sintering behavior of protonic perovskites.

Due to their different coordination environments with respect to oxygen-ion in the perovskite lattice, specific size requirements exist for both A-site and B-site cations. Typically, A-site cations are alkaline earth elements such as Ba, and lanthanum elements, while B-site cations are mainly selected from transition metal elements. Notably, certain cations, like Y^{3+} and Dy^{3+}, can be doped into both A and B-site of perovskite lattice.[10] In recent observations, we have noted a dynamic displacement of Y^{3+} between A and B-site at elevated temperatures, which has an adverse effect on the sintering of $BaZr_{0.1}Ce_{0.7}Y_{0.1}Yb_{0.1}O_{3-\delta}$ (BZCYYb), a representative protonic conducting perovskite electrolyte.[10a] Considering that the Y^{3+} doping level is merely 10% and the majority of cations at the B-site are Ce^{4+}, the thermal redox of Ce^{3+}/Ce^{4+} at elevated temperatures would also determine the sinterability of BZCYYb electrolyte. Specifically, Ce adopts a 4+ oxidation state and is doped into the B-site of perovskite lattice, as Ce^{4+} (0.87 Å, CN = 6) has been conventionally believed to be too small for the A-site.[11] However, when Ce^{4+} is thermally reduced to Ce^{3+} (1.34 Å, CN = 12) at the sintering temperature of protonic perovskites, i.e., 1200–1600 °C, the mismatched ionic radius would promote the partial replacement of Ce into the A-site.[12] It suggests the dynamic Ce displacement between A and B-site during high-temperature sintering has an impact on the sintering of Ce-rich perovskites. Indeed, amorphous Ba-rich layers at grain boundaries in sintered BCO polycrystals have been recently observed by an atomic-column-resolved imaging technique,[13] meanwhile, a certain amount of intermixing Ce was found to occupy the A-site at the bulk.[13–14] However, there is no further supporting evidence regarding the exact role of dynamic Ce redox in sintering of cerium-rich protonic perovskites.

Herein, through a systematic investigation based on the BCO perovskite, we observed the exsolution of cerium oxide from the perovskite lattice during high-temperature sintering, and the degree was affected by the powder synthesis method and the A to B cation stoichiometry. Such exsolution subsequently confirmed to originate from the thermal reduction of Ce^{4+} to Ce^{3+}. Previously, the poor sinterability of protonic electrolytes was attributed to the Ba evaporation. However, we surprisingly found that Ba deficiency actually promoted the densification and grain growth of BZO, while excess Ba had negative effects. On the contrary, in the case of BCO, Ba deficiency promoted the exsolution of CeO_2, while Ba excess suppressed such phenomena. The reason for such different behaviors is explained based on the thermal induced Ce exsolution (displacement) during the sintering. The knowledges as obtained then guided the fabrication of anode supported thin film BZCYYb cell, which delivered favorable performance. These findings provide new inspiration into the sintering of protonic perovskite electrolytes, which would foster new strategies for developing new electrolytes with improved sinterability for PCCs.

2. Results and Discussion

2.1. Observation of BaO and CeO_2 Segregation

The Ba evaporation at high temperatures was regarded as a key factor that influencing the sinterability of Ba-based perovskite electrolytes. Several independent groups have reported that the Ba loss was significant when the sintering temperature exceeds 1250 °C.[7a,15] Interestingly, at a temperature of 1500 °C, the partial pressure of gaseous BaO is $\approx 10^{-5}$ atm. Han et al. investigated that the partial pressure of gaseous BaO that decomposed from $BaZrO_3$ is very low, showing $\approx 10^{-9}$ atm the same temperature.[16] These findings indicate that during the sintering process, the actual loss of Ba through vaporization is minimal. In fact, in order to mitigate the potential Ba loss through evaporation, excess Ba was applied during the sintering, and an enclosed environment was created (through using a cover for the crucible). However, no obvious improvement in sintering was obtained in our experiments (Figures S4 and S5, Supporting Information). Meanwhile, some literatures revealed that excess Ba could be detrimental for the densification of BCO-BZO based perovskite electrolytes (Table S1, Supporting Information),[17] which suggests that new consideration unrelated to Ba evaporation should be explored.

Herein, we conducted a systematic and comparative investigation on the sintering of parent BZO and BCO at different temperatures from 1400 to 1600 °C, both powders were synthesized by solid-state reaction (SSR) method (Figures S1–S5, Supporting Information). As shown in Figure S6 (Supporting Information), the XRD patterns of BZO after sintering still showed a pure perovskite phase over the wide sintering temperature range without the appearance of any secondary phase. In the study of BCO series, a completely different phenomenon was observed. The XRD pattern of BCO pellet sintered at 1400 °C revealed a single-phase perovskite structure, while these characteristic peaks slightly shifted to higher degree when the sintering temperature increased to 1500 °C, indicating an abnormal lattice shrinkage instead of the expected thermal excitation-induced expansion at high temperatures.[18] It is important to highlight that some fluorite phase was also detected, which can be indexed based on CeO_2, suggesting the potential exsolution of CeO_2 from parent lattice during sintering at high temperatures.

For the BCO, it was found that the powder synthesis methods also had a big impact on the phase composition. The sol-gel method (SG) has been widely used to prepare ultrafine perovskite

powders at lower calcination temperatures.[19] However, synthesized BCO-SG powders exhibited a higher CeO_2 impurity content (Figure S1, Supporting Information), which can be attributed to the incompletely decomposed carbonaceous species in precursor. Specifically, reduced oxygen partial pressure caused by the combustion of chelating agents in the precursor inhibits the decomposition of $BaCO_3$, thereby promoting the CeO_2 exsolution from the perovskite lattice.

Interestingly, this CeO_2 phase was exclusively detected within the interior of the BCO-SG powder, rather than on the top surface where the loss of Ba is typically expected to be more significant (Figure S2, Supporting Information). In contrast, BCO-SSR sample synthesized at 1100 °C had a pure $BaCeO_3$ perovskite structure. Additionally, the XRD results also revealed that increasing O_2 partial pressure during the calcination process improved the phase purity of BCO-SG sample (Figure S1, Supporting Information), which is attributed to the elimination of carbonate species that are derived from the incomplete combustion of organic additives (Figure S3, Supporting Information). These findings suggest that the exsolution of CeO_2 may not be determined solely by the evaporation of Ba.

To further demonstrate whether the CeO_2 exsolution from BCO at elevated temperatures is primarily determined by the A-site deficiency from Ba evaporation during the sintering, the stoichiometric BCO powders were recalcined at various temperatures and subjected for comprehensive analysis, in which the physical information was collected by the synchrotron radiation facility with an energy of 17.501 keV. In the powder diffraction patterns, detailed information indicates that the segregation of CeO_2 secondary phases occurred only at temperatures >1400 °C (**Figure 1a**; Figure S7, Supporting Information), which is in accordance with the appearance of thermal reduction of Ce^{4+} to Ce^{3+}.[20] Apparently, the BCO powder recalcined at 1600 °C exhibited several new diffraction peaks associate with CeO_2, while crystalline Ba-species were not detected, in good agreement with the previous results.[21] To get information about the cation ratio in the various samples, they were subjected for inductively coupled plasma optical emission spectroscopy (ICP-OES) analysis. According to the results in Figure 1b, recalcined BCO powders still kept a stoichiometric ratio of Ba/Ce even after calcinating at 1600 °C, suggesting that BaO was actually not lost, instead it retained within the sample. In addition, we also compared the molar ratio of Ce/Ba in classic $BaZr_{0.4}Ce_{0.4}Y_{0.1}Yb_{0.1}O_{3-\delta}$ (BZCYYb-4411) perovskite to further confirm our findings. Specifically, the BZCYYb-4411 powders were stored in a lid-covered Al_2O_3 crucible and recalcined at 1600 °C for 10 h. The consistent Ce/Ba ratio equal to the theoretical value of 0.4 in both interior and exterior of the BZCYYb-4411 powder was observed, which indicates that the Ba evaporation in BZCYYb-4411 at 1600 °C was also negligible. It has been reported that excess Ba would aggregate at grain boundaries during sintering, consequently deteriorating the chemical stability and conductivity,[14] which was confirmed in this study on the basis of high-resolution transmission electron microscopy (HR-TEM) and time-of-flight secondary ion mass spectrometry (TOF-SIMS) analyses. As shown in Figure 1c, the HR-TEM images of the BCO powder recalcined at 1600 °C exhibited an amorphous layer covering the particle surface, which was further decorated with several nanoparticles with a lattice distance of 3.13 Å, corresponding to the segregated CeO_2 nanoparticles (Figure 1c). In comparison, BCO powder recalcined at 1400 °C presented a pure phase with the lattice distance of 3.11 Å, in consistence with the (211) diffraction plane of BCO as shown in Figure 1d. The scanning electron microscopy (SEM) image displayed several grain boundaries on the surface of layer-by-layer polished BCO pellet (Figure 1e). Note that higher signal of both Ba and O elements (Figure 1f–h) represents the aggregation of BaO species at grain boundaries. Apparently, stronger Ba signal surrounded the segregated Ce-rich particles, suggesting that the aggregation of Ba at grain boundaries was caused by the exsolution of Ce from lattice rather than thermodynamic evaporation. Figure S8 (Supporting Information) displays the X-ray photoelectron spectroscopy (XPS) spectra of O 1s and Ce 3d for CeO_2 calcined in O_2 or N_2 atmosphere at 1000 °C and then quenched to room temperature at the same atmosphere, the large amount of oxygen vacancies and Ce^{3+} species in N_2-treated CeO_2 confirms that Ce^{4+} can be easily reduced to Ce^{3+} at high temperature and low oxygen partial pressure (Tables S2 and S3, Supporting Information).

Considering the above experimental findings, we assume that the thermal reduction of Ce^{4+} to Ce^{3+} occurs during the high-temperature sintering (>1400 °C), which promotes the partial displacement of Ce from B-site to A-site with the oxidation state of Ce^{3+} and partial Ce is exsolved to form CeO_2 second phase. In addition, this mismatched occupation leads to the exsolution of Ba species from their original site, resulting in the formation of amorphous phases at grain boundaries. However, the reduced Ce^{3+} could also be partially re-oxidized to Ce^{4+} at low temperatures, which is too small to stay at the A-site, thereby further segregating the existence of CeO_2 clusters on surface to maintain the stoichiometry across all the sites in perovskites.

2.2. Detrimental Effect of Thermal Reduction of Ce^{4+} on Electrolyte Sintering

To investigate the effect of Ce^{4+} thermal reduction on the sintering behavior of protonic perovskites, BCO was selected and investigated. **Figures 2** and S9 (Supporting Information) exhibit the surface and cross-sectional SEM images of BCO pellets sintered at 1200–1600 °C, in which precursors were obtained via conventional SSR methods. As shown in Figure S9 (Supporting Information), BCO pellet sintered at 1200 °C presented a porous morphology, several micropores and connected channels were uniformly distributed within the pellet bulk and on the surface. In comparison, the higher sintering temperature of 1400 °C significantly improved the densification of BCO, the pellet showed a dense and clean surface, while trace amount of isolated pores was remained in the pellet interior (Figure 2a; Figure S9, Supporting Information), suggesting that the densification process was undergoing. However, further increasing the temperature brought negative effects on the sintering performance of BCO. For example, BCO pellet sintered at 1500 °C has a rough surface, showing that several nanoparticles were distributed along with grain boundaries (Figure 2b). The linear EDS scan spectrum and mapping images (Figure S10, Supporting Information) confirmed that these particles are segregated CeO_2, in good agreement with the XRD patterns shown in Figure S6 (Supporting Information). Obviously, the peeling off of segregated CeO_2 left a

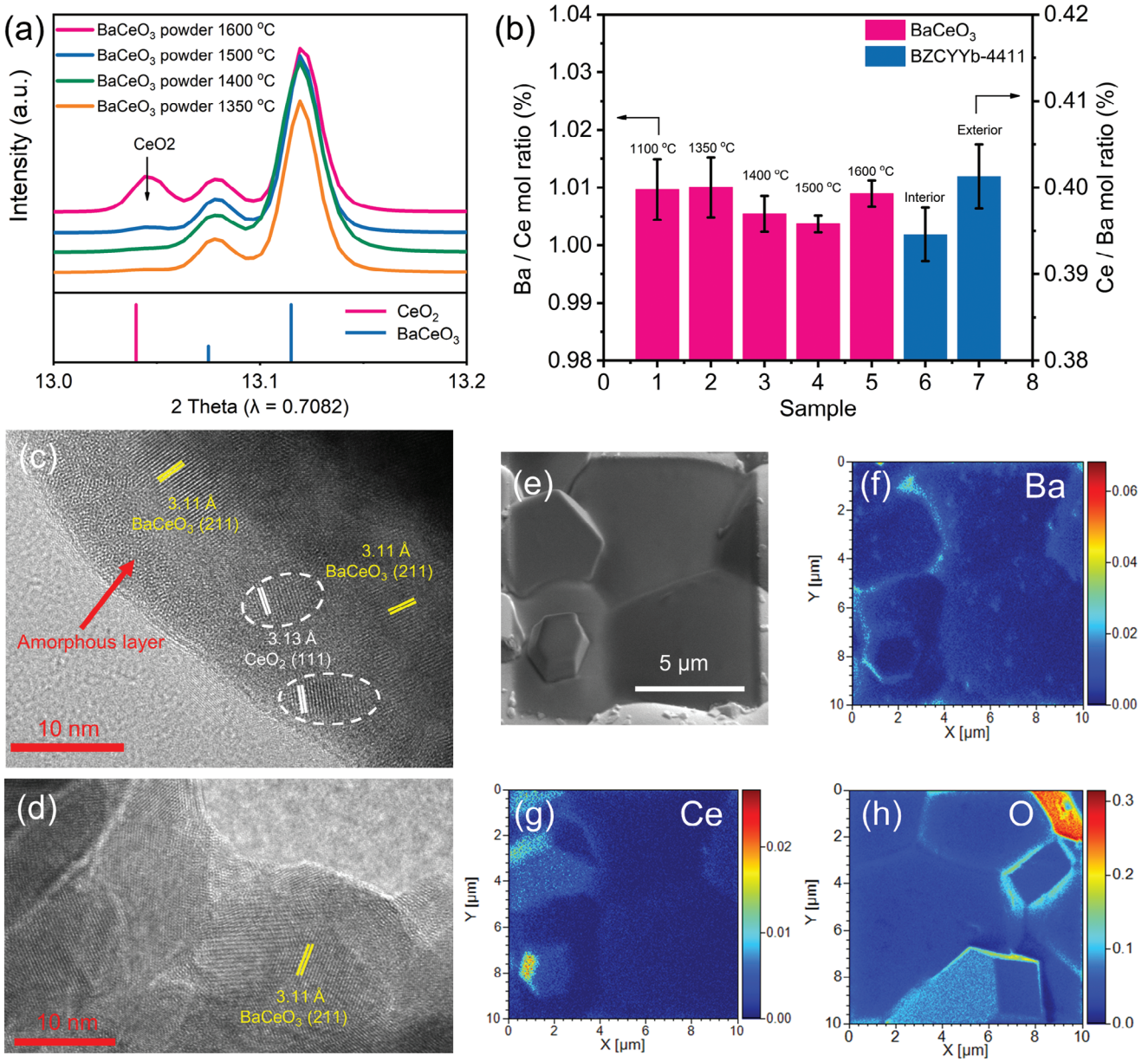

Figure 1. Observation of BaO and CeO_2 segregation in BCO samples calcined at elevated temperatures. a) Powder diffraction patterns with an X-ray energy of 17.501 keV of BCO powders recalcined at a temperature range of 1350–1600 °C in air. b) The comparison of Ba and Ce content in recalcined BCO and BZCYYb-4411 powders, all data was obtained by ICP-OES analysis. HR-TEM images of BCO powders recalcined at c) 1600 °C and d) 1400 °C. e) Surface SEM images of polished BCO pellets, which was calcined at 1600 °C for 5 h. The variated TOF-SIMS total intensity data of corresponding f) Ba, g) Ce, and h) O element at the polished surface.

pore at the original location (Figure S10, Supporting Information), proving that excess cation exsolution from lattice deteriorates the sinterability of perovskites. Meanwhile, it is clear that more pores on surface and in bulk region existed in BCO pellets sintered at 1600 °C. Previous studies suggest that the sinterability of Ba-based electrolytes could be intimately affected by the ionic radius of dopant elements, assuming that dopants with larger ionic radii than Ce^{4+} and Zr^{4+} are not conducive to the sintering.[10b,22] A comparison of sintering properties for BZCYYb and BZCY is shown in Figures S11 and S12 (Supporting Information), in which the BZCY pellet sintered at 1600 °C exhibited porous morphology along with segregated Y-rich clusters while the BZCYYb pellet was highly densified. This is a good indication of the improved sinterability by substituting Y^{3+} with a smaller cation such as Yb^{3+}. Interestingly, as shown in Figure S13 (Supporting Information), densified BZCYYb and BCO pellets became porous after heat-treating at 800 °C in a reduced atmosphere (10% H_2/Ar). In contrast, the morphology of the BZO pellet remained unchanged. Since the Ce^{4+} can be thermally reduced at elevated temperatures, larger Ce^{3+} would accelerate its

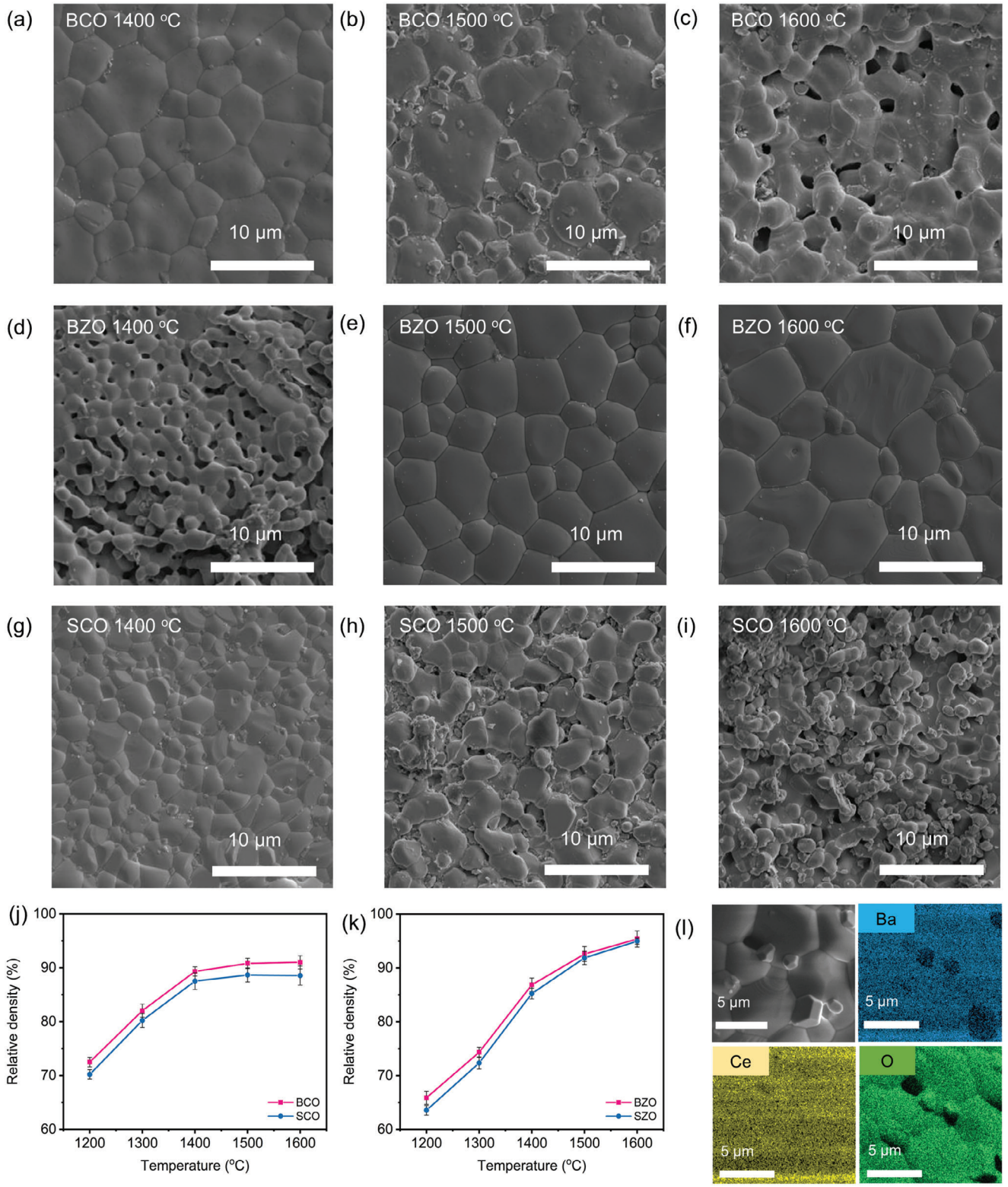

Figure 2. The sinterability of BCO and its comparison with other electrolyte materials. SEM images of the surface of a–c) BCO pellets, d–f) BZO pellets, and g–i) SCO pellets sintered at 1400–1600 °C, respectively. Relativity density of j) sintered BCO and SCO, k) BZO and SZO pellets at different temperatures. l) The surface SEM-EDX images of BCO pellet sintered at 1500 °C.

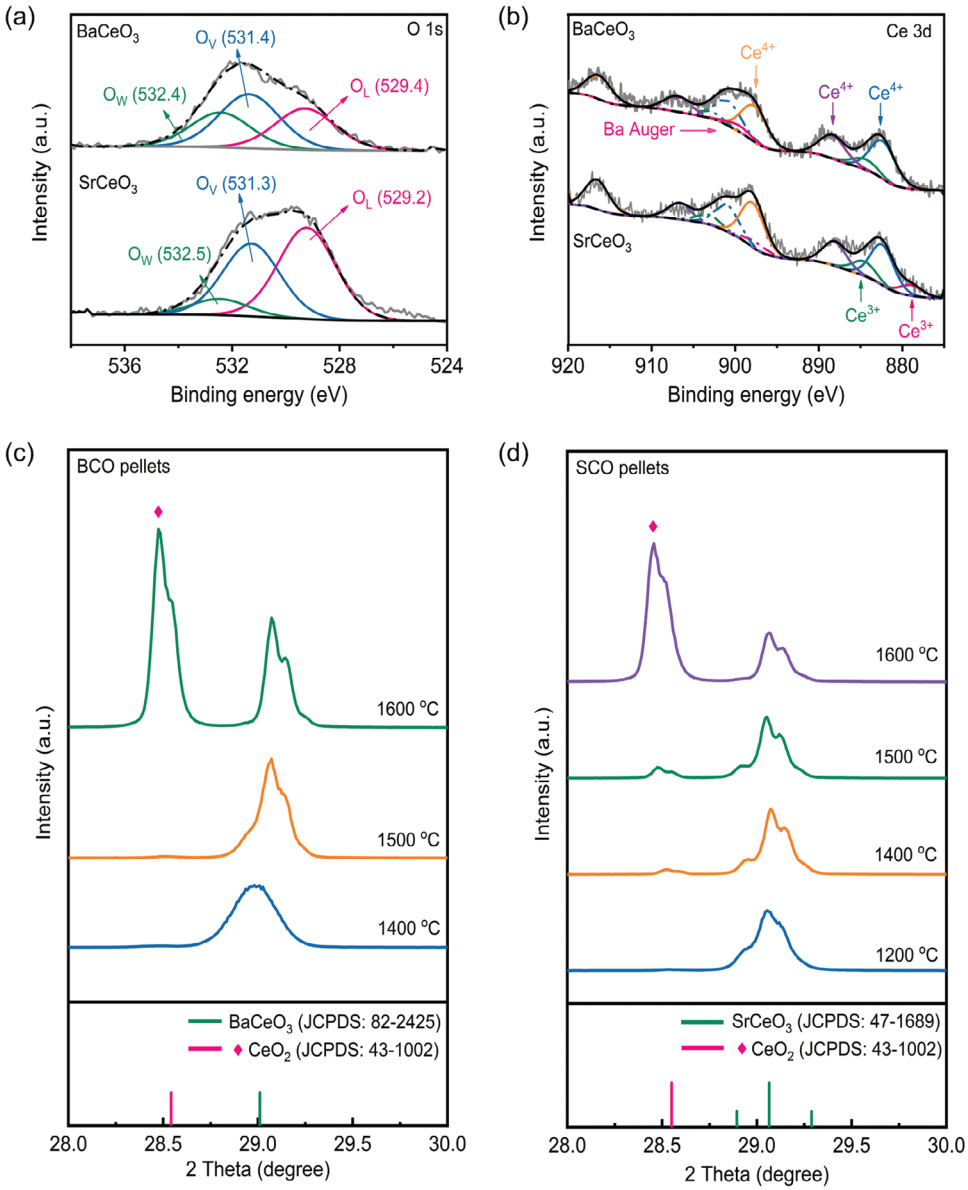

Figure 3. Structural characterization of BCO and SCO materials. a) O 1s and b) Ce 3d core-level XPS spectra of BCO and SCO, which were calcined at 1100 °C and quenched to room temperature. The XRD pattern of c) BCO and d) SCO pellets sintered at various temperatures.

dynamic displacement from original sites, which analogous to the movement of Y^{3+} in BZCY and BZCYYb. Consequently, the reduction of Ce plays an important role in undermining the densification of Ce-based perovskite electrolytes at high temperatures.

To gain an in-depth understanding of the influence of the Ce valence state change on the electrolyte sinterability, BZO and Sr-based perovskites, specifically $SrCeO_3$ (SCO) and $SrZrO_3$ (SZO), were also prepared using the SSR method. The SEM images of pellets sintered at 1400–1600 °C are presented in Figure 2. As anticipated, SCO pellets exhibited a similar sintering performance with BCO, showing porous surface after the sintering at 1500 °C (Figure 2g-i). The XRD result reveals that the formation of CeO_2 particles in SCO pellets started at 1400 °C (Figure S6b,c, Supporting Information), which is below the decomposition temperature for BCO, that is ≈1500 °C. Due to the smaller ionic radius of Sr^{2+} (1.44 Å) compared with Ba^{2+} (1.61 Å),[23] the reduced Ce^{3+} in SCO is more prone to migrate from B-site to A-site and exsolve as CeO_2.[19,20] The much smaller tolerance factor of 0.885 for SCO than that of 0.938 for BCO implies more serve distortion in SCO, which leads to drastic variation in the lattice structure and results in poor sinterability. The XPS spectra of quenched BCO and SCO are shown in **Figure 3**a,b, in which three peaks in O 1s spectrum can be assigned to lattice oxygen species (O_L, ≈592.3 eV), hydroxyl groups associate with lattice defects on surface (O_V, ≈531.4 eV) and adsorbed H_2O molecular (O_W, ≈532.4 eV).[24] It has been seen that the content of O_V species in SCO is significantly lower compared to BCO, while a higher

number of Ce^{3+} concentration was observed, which implies that some portion of reduced Ce^{3+} indeed migrated and occupied into the A-site as oxygen vacancies were consumed.[25] In the case of BZO, higher sintering temperature certainly enhanced its densification and grain growth (Figure 2d–f). The XRD results indicate that both BZO and SZO have superior thermal stability even if the sintering temperature exceeded 1600 °C (Figure 6d–f, Supporting Information). It is well known that the oxidation state of Zr cation in oxides is considered as constant as Zr^{4+}.[26] Thus, the dynamic displacement of Zr^{4+} from B to A-site is negligible as its ionic radius is too small for the A-site in comparison with Ba^{2+} or Sr^{2+}.

The volume shrinkage and relative density of BCO, BZO, SCO and SZO pellets after the sintering at the temperature range of 1200–1600 °C are shown in Figure 2j,k; Figure S14 and Table S6 (Supporting Information). The BCO pellet sintered between 1200 and 1400 °C demonstrated a sharply increased volume shrinkage rate from 17.6% to 43.6% and the increased relative density from 72.5% to 89.3%, respectively. However, the relative density of BCO was kept at ≈91% when the sintering temperature further increased to 1600 °C. Similarly, the relative density of SCO pellets enhanced to 87.5% after sintering at 1400 °C, while steadily varied at ≈88% after sintering at 1500 and 1600 °C. This result strongly indicates that sintering temperature >1500 °C is not necessary for the densification of BCO electrolyte. In comparison, the BZO and SZO exhibited an increased sinterability with the enhanced sintering temperature, and the relative density of BZO and SZO reached 95.4% and 95.0% after sintering at 1600 °C, respectively.

The solid-state sintering at high temperatures involves the mass transport below the material melting point, which is typically driven by the surface chemical potential. The grain growth, or called densification, primarily determined by the atom diffusion from grain boundaries to the neck surface between two connected particles, which decreases the total surface area of compacted powders. At the initial stage, the ions should have sufficient mobility to trigger sintering. To improve the ion mobility, several strategies such as introducing vacancies and low-melting liquid phase have been documented as effective means to reduce the sintering temperature of densified perovskite electrolytes.[22,27] However, the surface diffusion near a pore only contributes to the changes in particle shape (coarsening) while leaving pores intact.[28] Generally, the densification of solid materials is driven by the grain boundary diffusion, accompanied by the vanishment of particle interfaces.[28,29] Owing to the lattice distortion occurred by the Ce reduction, Ce species have a potential to diffuse to particle surface and destabilize the perovskite lattice (illustrated in **Figure 4a**), rather than incorporate the grain growth, therefore inhibiting the densification of $BaCeO_3$-based electrolytes. Density functional theory (DFT) calculations indicate that Ce in $BaCeO_3$ exhibits a lower surface segregation energy than Zr in $BaZrO_3$ (Figure 4c), which suggests that Ce is more likely to segregate from the lattice to the surface. As shown in Figure 4d, the energy barrier for the Ce mismatched occupation at A-site in $BaCeO_3$ was calculated to be 2.90 eV, lower than that on the Zr displacement in $BaZrO_3$ (7.12 eV), consisting with the experimental results, which further supports an adverse effect of Ce reduction on the electrolyte sinterability. Furthermore, the electronic structure of BCO and BZO was calculated to gain insights into the thermal reduction behavior of Ce in perovskite materials. Figure 4e,f exhibits the electronic work function of BCO and BZO, respectively, which represents the minimum energy required for an electron to escape from the material lattice to a point outside material surface. The lower energy demand of 3.936 eV in BCO compared to 4.523 eV in BZO suggests the faster electron transfer in BCO.[30] Additionally, the electrostatic potential distribution of BCO and BZO was assessed by calculating their electrostatic potential maps (Figure 4g,h), where yellow and blue regions represent the positive and negative electrostatic potential, respectively.[31] Notably, in the case of BCO, the Ce-sites displayed a more positive electrostatic potential compared to the Zr-sites in BZO, indicating that Ce is more favorable for attracting negatively charged species such as electron.[31]

2.3. Improving the Sinterability of Ba-Based Electrolytes

Given the positive effect of controlling the Ba content on the electrolyte sintering, we further conducted a comparative study on the sinterability of BCO and BZO with a 5% Ba variation. Considering that the reduced Ce^{3+} can potentially migrate to the A-site, deliberately introducing excess Ba has a potential to inhibit this mismatched occupation. Specifically, Ba-rich, stoichiometric, and Ba-deficient BCO and BZO powders were sintered at 1100 °C for 10 h, followed by quenching to room temperature to keep their high-temperature lattice structure. To ascertain the impact of Ba content on suppressing the Ce migration, we examined the Ce valence state change in three quenched BCO samples using Ce L_3-edge X-ray absorption spectroscopy (XAS), as shown in **Figure 5e**. Note that both Ba deficient and stoichiometric BCO powders exhibited a shoulder-peak at ≈5725 eV, which can be ascribed as the transition from Ce 2p core level to Ce $4f^1 5d$, indicating the presence of Ce^{3+} in the quenched samples.[32] In the case of Ba-rich BCO sample, a slight peak at ≈5737 eV was assigned to the transition of Ce 2p to Ce $4f^0 5d$ final state, which represents the Ce^{4+} oxidation state.[33] Meanwhile, the minor spectrum weight shift of Ba-deficient BCO toward lower energies also indicates the decrease in valence state of Ce. In comparison, the enhancement of Ce valence in Ba-rich BCO was also confirmed according to the spectrum weight shift proceed to higher energies. Therefore, we demonstrated that introducing excess Ba has a benefit in inhibiting Ce reduction during the high-temperature calcination. In addition to the valence state variation of Ce, the XRD results (Figure 5c; Figure S17, Supporting Information) of quenched BCO samples reveal that both Ba deficient and stoichiometric powders had slight peak shifts toward to lower degree. The expansion of their cell volume indicates the minor reduction of Ce^{4+} at the B-site during the calcination. In stoichiometric BCO, the orthorhombic BCO phase with lattice parameters of a = 8.8288, b = 6.1987, and c = 6.2153 Å and cell volume of 340.1464 $Å^3$ was calculated based on the Rietveld XRD refinement (Figure S18 and Table S7, Supporting Information), while $Ba_{1.05}CeO_3$ and $Ba_{0.95}CeO_3$ possessed cell volume of 339.8870 and 340.2506 $Å^3$, respectively. Obviously, insufficient Ba also promoted the segregation of Ce from lattice, showing 2.35 wt% of CeO_2 phase in the Ba-deficient BCO composites (Figure S18d, Supporting Information). As demonstrated in XPS spectra of O 1s and Ce 3d core levels of Ba-deficient and Ba-rich BCO (Figure 5d; Figure S19 and

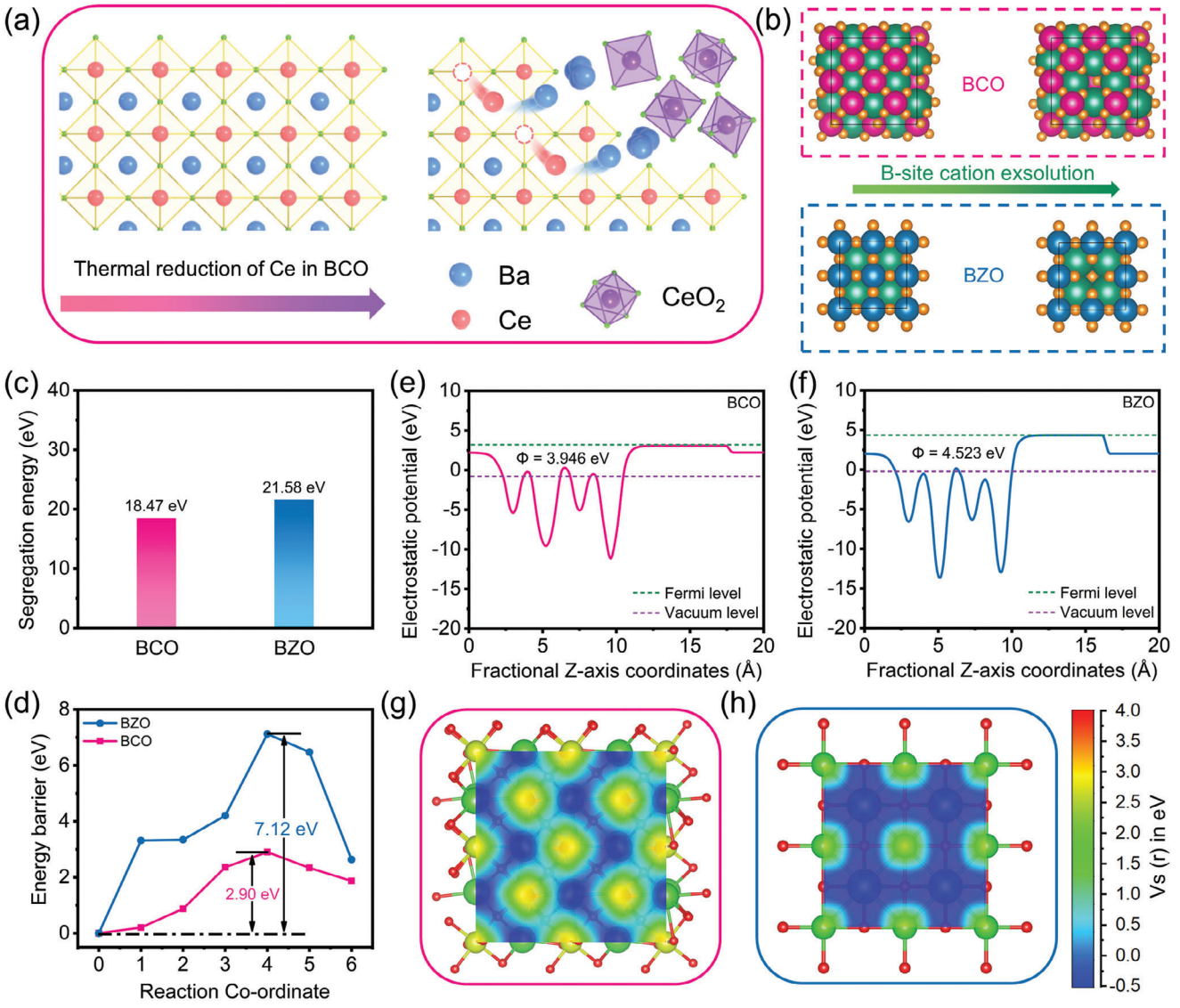

Figure 4. DFT calculations of Ce and Zr displacement behavior in Ba-based perovskites. a) The schematic illustration represents the dynamic displacement of reduced Ce from the B-site to the A-site and the resulting segregation of CeO_2 and Ba species from the perovskite lattice. b) Diagram of the B-site cation exsolution from lattice, in which red, blue, green, and yellow ball represents the Ce, Zr, Ba, and O atom, respectively. c) The calculated segregation energy of Ce from $BaCeO_3$ and Zr from $BaZrO_3$, respectively. d) The energy barrier of Ce and Zr occupation at the A-site (Ba). The work functions of e) $BaCeO_3$ and f) $BaZrO_3$, respectively. The calculated electron-density isosurface of g) $BaCeO_3$ and h) $BaZrO_3$, respectively. The electron-density isosurface was plotted at 0.001 e $bohr^{-3}$. The color bar represents the scale of electrostatic potential.

Table S8, Supporting Information), partial A-site deficiency enhanced the amount of O_V (57.2%) and Ce^{3+} percentage (13.5%) in BCO. As suggested above, the reduction of Ce^{4+} generates additional defects if the Ce^{3+} still keeps at the B-site, which can be illustrated as follow:

$$2Ce_{Ce}^{X} + O_{O}^{X} \rightleftarrows 2Ce_{Ce}^{'} + V_{O}^{\cdot\cdot} + \frac{1}{2}O_2 \quad (1)$$

In an attempt to maintain the stoichiometric structure in an A-site-deficient perovskite, the introduced oxygen vacancies further destabilize the lattice structure, thereby facilitating the exsolution of B-site species.[34] By contrast, Ba-rich BCO shows a single-phase structure, all characteristic peaks are located at the theoretical position. The XPS results delivery a declined content of both O_V (17.3%) and Ce^{3+} (7.6%) in Ba-rich BCO, proving that the displacement of Ce species is also determined by the non-stoichiometry of perovskites. Specifically, excess Ba can react with reduced or segregated Ce species to reestablish perovskite lattice, thus improving the sinterability of BCO based electrolytes. Interestingly, the XRD pattern of BZO-based samples exhibits a contrary phenomenon. All characteristic peaks of perovskite phase in BZO samples with different Ba content are located at the theoretical position without peak shift (Figure 5c; Figure S17, Supporting Information), in good agreement with the truth that Zr^{4+} is difficult to be reduced. In Ba-rich and stoichiometric BZO samples,

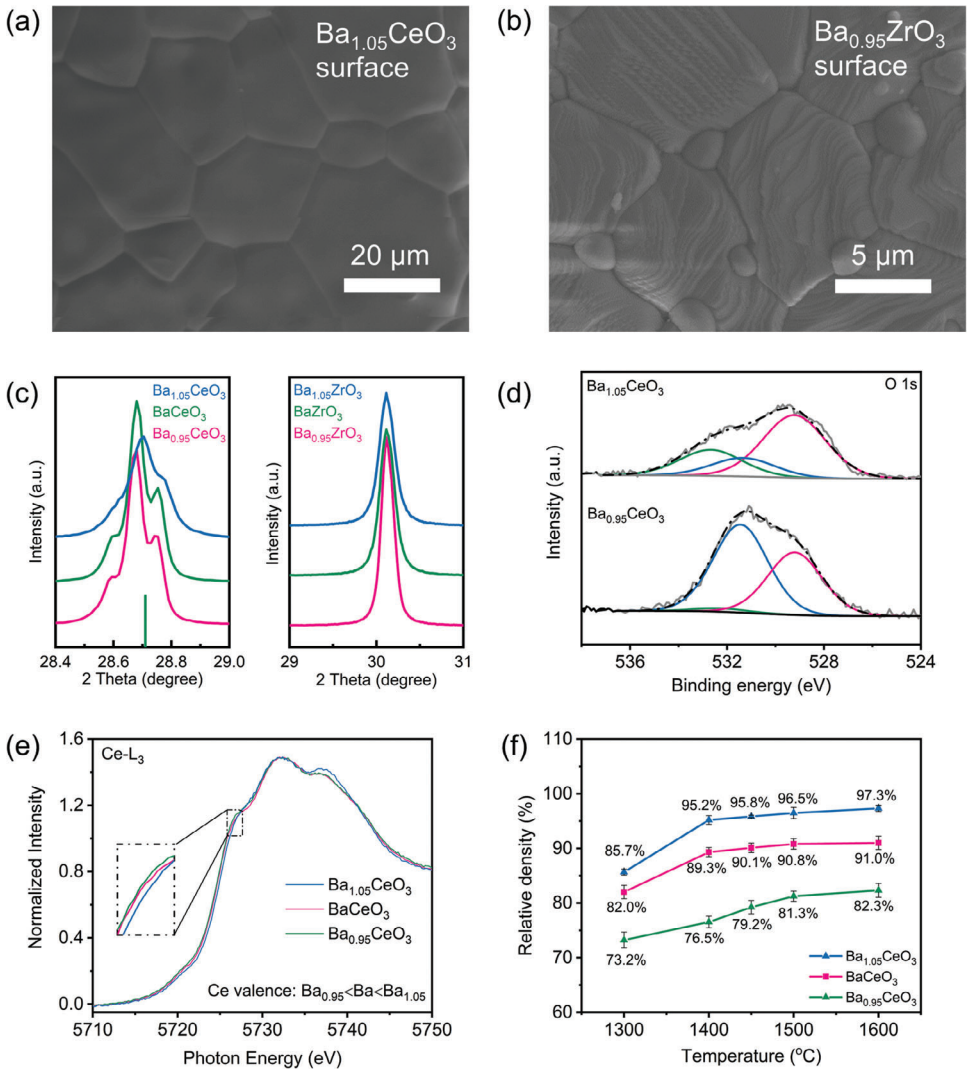

Figure 5. Improved sinterability of BCO and BZO electrolyte materials by adjusting Ba content. SEM images of the surface of a) Ba-rich BCO pellet sintered at 1450 °C and b) Ba-deficient BZO pellet sintered at 1600 °C. c) The XRD pattern of various BCO and BZO powders, which were calcined at 1100 °C and quenched to room temperature. d) O 1s core level XPS spectra and e) Ce L_3-edge XAS spectra of quenched stoichiometric, Ba-deficient, and Ba-rich BCO powders. f) The measured relative density of BCO pellets with different Ba content.

several small peaks corresponding to the $BaCO_3$ were observed, which may derive from the unreacted precursor.

To evaluate the effect of controlling the Ba content on the sinterability of BCO and BZO, the surface morphology of several sintered pellets was investigated by SEM analysis (Figures S20 and S21, Supporting Information). It is clear that the Ba-rich BCO (Figure 5a) and the Ba-deficient BZO (Figure 5b) pellets have improved densification and grain growth in comparison with other samples. Notably, the Ba-rich BCO pellet exhibited a clean and dense surface with the largest grain size of ≈20 μm, while several pores can be easily found in the Ba-deficient and stoichiometric BCO pellets (Figure S20, Supporting Information). The relative density of Ba-rich, stoichiometric, and Ba-deficient BCO sintered at 1450 °C are 95.8%, 90.1%, and 79.2%, respectively (Figure 5f), confirming that suppressing Ce^{3+} displacement has a positive effect on the electrolyte sintering. Surprisingly, excess Ba content limited the densification of BZO pellets as the Ba-rich sample had the lowest relative density of 87.5% than that of the Ba-deficient and stoichiometric BZO (Figure S22, Supporting Information). In comparison, the Ba-deficient BZO had the largest grains of about 5–10 μm and highest relative density of 98.2% (Figure S21, Supporting Information) although small amount of segregated secondary phase of ZrO_2 was observed (Figure S21g–i, Supporting Information), which is similar with the reported results that partial A-site deficiency facilitates the densification of Ba-based perovskites by enhancing the A-site cation diffusion rate.[8b,9] Consequently, we confirm that controlling the Ba content is a facile way for fabricating dense electrolyte. For composite electrolytes possess more Ce content, it is necessary to suppress the displacement of Ce^{3+} by adding more Ba species in precursor. On the contrary, Zr-rich electrolytes require slight Ba deficiency to promote sintering.

In addition to the cation stoichiometry, we revealed that the electrolyte sintering was also determined by the precursor

synthesis method. Specifically, BCO-based electrolytes have worse sinterability when precursors synthesized by SG method is conducted, which can be attributed to the incompletely decomposed carbonaceous species in precursor and the low packing density of compressed pellets.[35] (Figures S1–S5, Supporting Information).

2.4. Cell Performance

Based on above analysis, we choose conventional BZCYYb as electrolytes to prepare single cell and investigate the influence of sinterability on performance output. An ideal PCC should have thin and dense electrolyte to achieve high proton conductivity and prevent fuel penetration. **Figure 6**a,b shows cross-sectional SEM images of anode-supported single cells, in which electrolytes were fabricated by sintering BZCYYb precursors synthesized via SSR method (BZCYYb-SSR) and SG method (BZCYYb-SG), respectively. It should be noted that the BZCYYb-SSR electrolyte had better sinterability than that of the BZCYYb-SG electrolyte, showing higher OCV of 1.04, 1.06, 1.08, and 1.09 V at 600, 550, 500, and 450 °C, respectively (Figure 6c). In comparison, the inferior OCV of 1.01 V at 600 °C in BZCYYb-SG-based single cell is attributed to the intrinsic pores and cracks within electrolyte, which inevitably results in gas leakage during cell operation. Additionally, the BZCYYb-SSR-based cell also delivered enhanced peak power densities (PPDs) of 712.5 and 176.3 mW cm^{-2} at 600 and 450 °C respectively, while the BZCYYb-SG-based cell has much lower PPDs of 365.9 and 101.8 mW cm^{-2} measured at the same operation temperatures (Figure 6d; Figure S23a, Supporting Information). In order to avoid the influence of external factors such as electrode composition and electrolyte thickness, the preparation of both cells was carefully controlled under the same conditions. According to the electrochemical impedance spectroscopy (EIS) results (Figure 6e,f), BZCYYb-SSR cell showed reduced ohmic resistance (R_{hom}) of 0.19 Ω cm^2 at 600 °C than that of 0.39 Ω cm^2 in BZCYYb-SG cell, which should be ascribed as the eliminated structural defects and inhibited cation segregation (Figure 6a,b; Figure S26, Supporting Information). Note that two cells showed similar activation energies calculated by fitting R_{hom} at different temperatures (Figure 6g), which indicates the same proton conduction mechanism in two electrolytes. Meanwhile, two specific cells with different electrolytes have similar charge transfer resistance (R_{ct}), as shown in Figure 6c,d and Figure S23b (Supporting Information). The distribution of relaxation times (DRT) analysis shows that peaks representing different polarization processes in both cathode and anode had similar peak positions and intensities (Figure 6h; Figure S23c,d, Supporting Information), suggesting a high comparability of the cell fabrication. Therefore, it reveals that the inferior performance of BZCYYb-SG cells is mainly attributed to the high ohmic resistance (R_{hom}) derived from the poor densification.

3. Conclusion

In summary, we demonstrated a strong correlation between the thermal reduction of Ce^{4+} and the densification of BCO-based electrolytes. For the proof-of-concept study, we first compared the sinterability of Ba or Sr-based perovskites, revealing that the poor sinterability of conventional electrolytes is not related to the Ba evaporation while mainly caused by the nature of B-site cations. The results implied that the dynamic displacement of Ce^{3+} to the A-site not only leads to the exsolution of amorphous Ba-species at grain boundaries, but also deteriorates the densification of perovskites. As the thermal reduction of Ce^{4+} during high temperature sintering may be inevitable, deliberately introducing additional Ba source can significantly inhibit the Ce^{3+} misplaced occupation, which is a facile way for fabricating densified BCO electrolytes. Meanwhile, for materials contain a large amount of Zr, it is necessary to introduce the A-site deficiency. Therefore, controlling the Ba content is a compromise trade-off for preparing densified proton-conducting electrolytes. In addition, we revealed that the precursor synthesis method also influences the densification of BCO and BZO based electrolytes, showing that the fabricated single cell utilizing BZCYYb-SSR electrolyte possesses better sinterability and cell performances, which provides a new insight for developing high-performance PCCs.

4. Experimental Section

Materials Fabrication: BCO, BZO, SCO, SZO, and BZCYYb-SSR materials were synthesized using the conventional SSR method to prevent the influence of carbonate introduced by SG method on sintering, which is discussed in Supporting Information. For a typical preparation of BCO, stoichiometric amounts of $BaCO_3$ and CeO_2 powders were mixed with isopropanol and ball milled for 10 h with an yttria stabilized zirconia milling media. After drying the mixture at 80 °C for 12 h, the collected powder was calcined at 1100 °C for 10 h in the muffle furnace with ambient air, named as BCO. To control particle sizes of the final samples, all calcined powders were hand milled with a mortar and pestle and processed with a stainless sieve (160 mesh). In addition, $BaCo_{0.4}Fe_{0.4}Zr_{0.1}Y_{0.1}O_{3-\delta}$ (BCFZY) cathode, BCO-SG, BZO-SG, SCO-SG, SZO-SG, and BZCYYb-SG powders were synthesized through the SG method. Specifically, stoichiometric metal nitrates were dissolved into deionized water and heated at ≈125 °C, followed by dissolving ethylenediaminetetraacetic acid and citric acid (molar ratio to total cations of 1 and 2, respectively) with continuous stirring. A proper amount of ammonia water was added to adjust the solution pH to ≈7. After removing the majority of solution, sticky gel was transferred to a muffle furnace and calcined at 250 °C for 5 h, which was further calcined at 1000 °C for 5 h to obtain fine powders. In order to completely remove gaseous products, comparative samples were calcined in a tube furnace with a constant O_2 flow of 500 SCCM.

The as-obtained BCO, BZO, SCO, and SZO precursors were pressed into pellets to investigate their sintering properties. Generally, synthesized powders were mixed with a certain amount of PVA solution to enhance the mechanical strength of pressed green pellets. After that, 0.5 g powders were pressed into 15 mm diameter pellets with a pressure of 8 MPa, followed by calcining at the temperature range of 1200–1500 °C for 5 h. The volume and diameter shrinkage rate of all pellets were calculated by comparing the change of measured thickness and diameter before and after sintering process. In addition, the relative density of as-obtained pellets was measured by Archimedes method.

Materials Characterizations: The physical information of all synthesized samples was collected via powder XRD (D8 advance diffractometer, Bruker) with Cu-Kα source at 40 kV and 40 mA and powder diffraction utilizing synchrotron radiation with a beamline energy of 17.501 keV. The XPS analysis was performed on the ESCALAB 250Xi (Thermo Fisher Scientific). The Ce L_3-edge XAS data of quenched BCO samples were collected at the TLS 16A beamline, NSRRC, Taiwan. The surface and cross-section features of obtained pellets were performed through the SEM analysis (Clara, Tescan). Chemical compositions of powder samples were determined by the ICP-OES with Avio 550 Max (PerkinElmer). To investigate the Ba aggregation in sintered pellets, the TOF-SIMS technique was selected (LYRA3, Tescan). The attenuated total reflection Fourier transform infrared spectra were obtained from the Nicolet 510 spectrometer. To investigate the

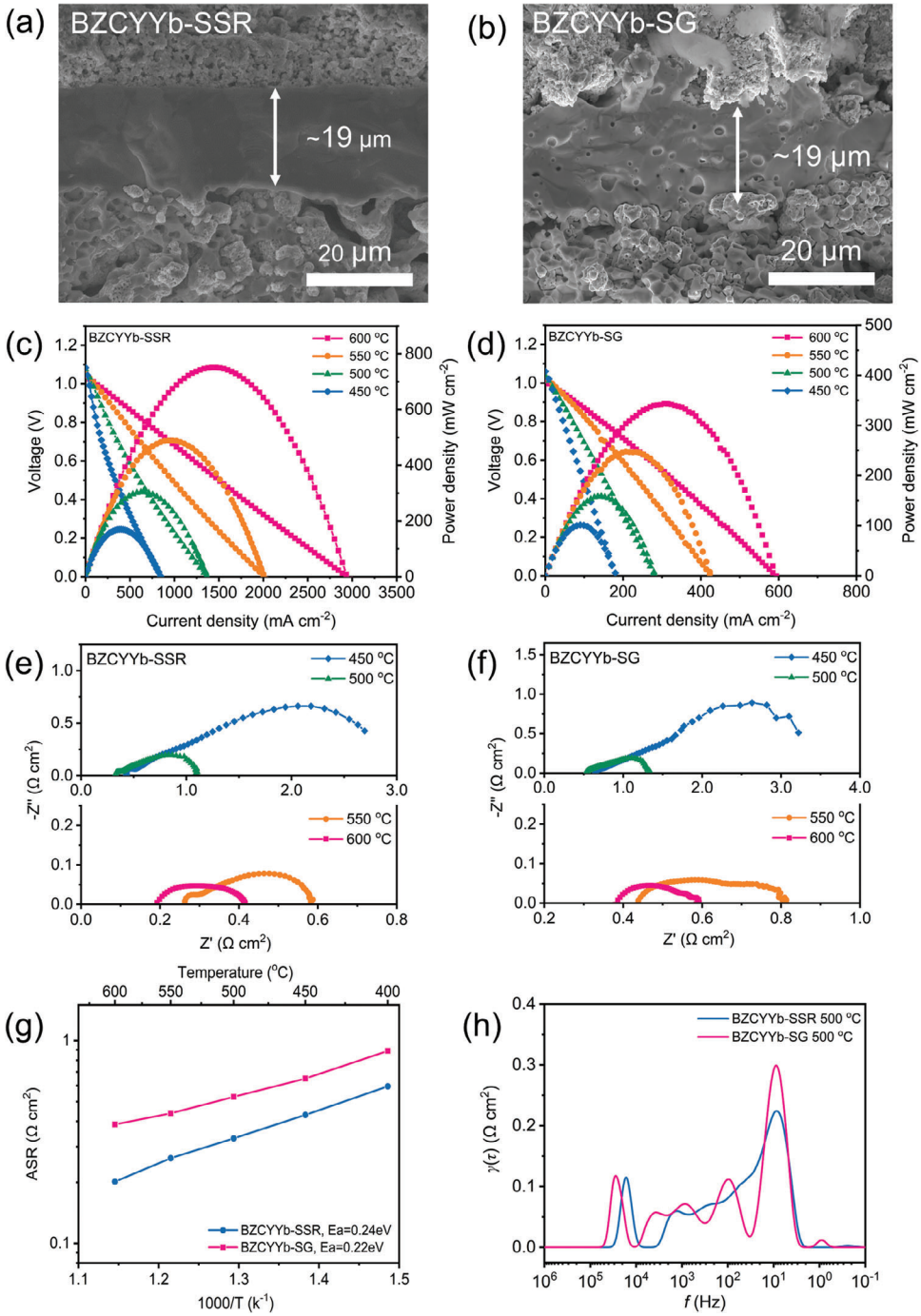

Figure 6. Enhanced electrochemical performance of BZCYYb single cells associated with improved electrolyte sinterability. Cross-sectional SEM images of BZCYYb-based single cells with a) BZCYYb-SSR and b) BZCYYb-SG as the electrolyte. *I–V* and *I–P* curves and EIS data of c,e) BZCYYb-SSR and d,f) BZCYYb-SG single cells measured at the temperature range of 450–600 °C, respectively. The comparison of g) aera specific resistance (ASR) of R_{ohm} and f) DRT analysis of two typical single cells tested at 500 °C.

carbonate content of as-prepared powder samples, the temperature programmed decomposition technique was combined with a mass spectrometer (ChemBET-3000, Quantachrome Instruments and ThermoStar GSD 301, Pfeiffer Vacuum). Typically, 50 mg powder sample was added into a U-type quartz tube, which was fed with pure argon with the gas flow rate of 20 SCCM. The temperature was increased from room temperature to ≈1000 °C with the ramping rate of 15 °C min^{-1}, and the exhaust gas was collected and analyzed by a MS instrument.

DFT Calculations: All DFT calculations for periodic material systems were performed using the Vienna Ab initio simulation package (VASP), employing the projector-augmented wave (PAW) method.[36] The exchange–correlation function was handled using the

generalized gradient approximation (GGA) formulated by the Perdew–Burke–Ernzerhof (PBE).[37] The van der Waals (vdW) interactions were described using the DFT-D3 method in Grimme's scheme.[38] For a better description of Ce electrons, the effective U value was set to 4.5 eV. The interaction between the atomic core and electrons was described using the projector augmented wave method. A plane-wave basis set energy cutoff of 500 eV was ultilized.[39] The Brillouin zone was sampled with a 3 × 3 × 1 grid centered at the gamma (Γ) point for geometry relaxation. To ensure negligible lateral interaction of adsorbates, all slabbed models had a vacuum spacing of ≈15 Å.[40] The bottom layers, comprising approximately half of the structure, were kept frozen at the lattice position.[41] All structures with dynamic magnetic moment were fully relaxed were fully relaxed without any restriction until their total energies converged to $<1 \times 10^{-6}$ eV,[42] and the average residual forces were <0.02 eV $Å^{-1}$.[43] Transition states were searched for using the climbing image nudged-elastic-band (CI-NEB) method, with convergence to 0.05 eV $Å^{-1}$ and $<2 \times 10^{-5}$ eV.

Fuel Cell Fabrication and Electrochemical Measurements: BZCYYb single cells were fabricated by spray coating and co-sintering method based on anode-supported pellets. Typically, for the fabrication of anode, BZCYYb-SSR raw material, NiO powder and starch in a weight ratio of 6:4:1 were homogeneously mixed with ethanol and dried at 80 °C for 12 h. Subsequently, collected powders were further mixed with PVA binder and then pressed into pellets. Lately, these green pellets were calcined at 450 °C and cooled down to room temperature to remove PVA binder, which was followed by spraying electrolyte slurry (a mixture of electrolyte powder, glycerol, ethylene glycol and ethanol) on pellet surface. The prepared anode-supported half cells were sintered at 1450 °C for 5 h to achieve sufficient electrolyte densification. The BCFZY cathode with ≈0.45 cm^2 area was sprayed onto the electrolyte side, and co-sintered at 1000 °C for 2 h.

Each single cell was heated up to 800 °C with a ramping rate of 5 °C min^{-1} and maintained for several hours to sufficiently reduce NiO component in anode. All electrochemical test of single cells were conducted at a temperature range of 450–600 °C. At the same time, dry H_2 was passed into the anode at a constant flow rate of 200 mL min^{-1} while the cathode was exposed to the ambient air. The EIS data was collected under OCV conditions with a frequency range of 10^6–10^{-1} Hz and an a.c. amplitude of 10 mV.

Supporting Information

Supporting Information is available from the Wiley Online Library or from the author.

Acknowledgements

This work is supported by the Australian Research Council Discovery Projects, grant Nos. DP200103315, DP200103332 and DP230100685. Authors acknowledge support from the Max Planck-POSTECH-Hsinchu Center for Complex Phase Materials, and the John de Laeter Centre for instrument provision and training.

Open access publishing facilitated by Curtin University, as part of the Wiley - Curtin University agreement via the Council of Australian University Librarians.

Conflict of Interest

The authors declare no competing interests.

Data Availability Statement

The data that support the findings of this study are available from the corresponding author upon reasonable request.

Keywords

cerium displacement, electrolyte sintering, protonic ceramic cells

Received: February 13, 2024
Revised: March 20, 2024
Published online: April 9, 2024

[1] S. Wang, S. P. Jiang, *Natl. Sci. Rev.* **2017**, *4*, 163.
[2] G. Yang, C. Su, H. Shi, Y. Zhu, Y. Song, W. Zhou, Z. Shao, *Energy Fuels* **2020**, *34*, 15169.
[3] T. Raza, J. Yang, R. Wang, C. Xia, R. Raza, B. Zhu, S. Yun, *Chem. Eng. J.* **2022**, *444*, 136533.
[4] J. Cao, Y. Ji, Z. Shao, *Energy Environ. Sci.* **2022**, *15*, 2200.
[5] a) C. Duan, R. J. Kee, H. Zhu, C. Karakaya, Y. Chen, S. Ricote, A. Jarry, E. J. Crumlin, D. Hook, R. Braun, N. P. Sullivan, R. O'Hayre, *Nature* **2018**, *557*, 217; b) L. Yang, S. Wang, K. Blinn, M. Liu, Z. Liu, Z. Cheng, M. Liu, *Science* **2009**, *326*, 126.
[6] a) F. Liu, H. Deng, D. Diercks, P. Kumar, M. H. A. Jabbar, C. Gumeci, Y. Furuya, N. Dale, T. Oku, M. Usuda, P. Kazempoor, L. Fang, D. Chen, B. Liu, C. Duan, *Nat. Energy* **2023**, *8*, 1145; b) W. Bian, W. Wu, B. Wang, W. Tang, M. Zhou, C. Jin, H. Ding, W. Fan, Y. Dong, J. Li, D. Ding, *Nature* **2022**, *604*, 479.
[7] a) A. Magrez, T. Schober, *Solid State Ion* **2004**, *175*, 585; b) M. Choi, J. Paik, D. Kim, D. Woo, J. Lee, S. J. Kim, J. Lee, W. Lee, *Energy Environ. Sci.* **2021**, *14*, 6476.
[8] a) S. M. Choi, J.-H. Lee, J. Hong, H. Kim, K. J. Yoon, B.-K. Kim, J.-H. Lee, *Int. J. Hydrog. Energy* **2014**, *39*, 7100; b) Y. Guo, R. Ran, Z. Shao, S. Liu, *Int. J. Hydrog. Energy* **2011**, *36*, 8450.
[9] H. Zhao, Y. Cheng, N. Xu, Y. Li, F. Li, W. Ding, X. Lu, *Solid State Ion* **2010**, *181*, 354.
[10] a) Z. Liu, Y. Song, X. Xiong, Y. Zhang, J. Cui, J. Zhu, L. Li, J. Zhou, C. Zhou, Z. Hu, G. Kim, F. Ciucci, Z. Shao, J.-Q. Wang, L. Zhang, *Nat. Commun.* **2023**, *14*, 7984; b) D. Han, Y. Nose, K. Shinoda, T. Uda, *Solid State Ion.* **2012**, *213*, 2.
[11] R. Shannon, *Acta Crystallogr.* **1976**, *32*, 751.
[12] a) D. Liu, Y. Dou, T. Xia, Q. Li, L. Sun, L. Huo, H. Zhao, *J. Power Sources* **2021**, *494*, 229778; b) R. Woo, K. Lee, B.-S. An, S. H. Kim, H. Ju, J. H. Kim, J. Shim, H.-T. Beum, K. Cho, Y.-S. Bae, H. C. Yoon, *Chem. Eng. J.* **2023**, *475*, 146354; c) F. He, Z. Teng, G. Yang, C. Zhou, D. Guan, S. Chen, R. Ran, W. Wang, W. Zhou, Z. Shao, *J. Power Sources* **2020**, *460*, 228105; d) F. He, Q. Gao, Z. Liu, M. Yang, R. Ran, G. Yang, W. Wang, W. Zhou, Z. Shao, *Adv. Energy Mater.* **2021**, *11*, 2003916.
[13] H.-S. Kim, J.-S. An, H. B. Bae, S.-Y. Chung, *Nat. Commun.* **2023**, *14*, 2255.
[14] H.-S. Kim, H. B. Bae, W. Jung, S.-Y. Chung, *Nano Lett.* **2018**, *18*, 1110.
[15] a) B. Bendjeriou-Sedjerari, J. Loricourt, D. Goeuriot, P. Goeuriot, *J. Alloys Compd.* **2011**, *509*, 6175; b) H. Dai, H. Kou, H. Wang, L. Bi, *Electrochem. Commun.* **2018**, *96*, 11.
[16] D. Han, Y. Otani, Y. Noda, T. Onishi, M. Majima, T. Uda, *RSC Adv.* **2016**, *6*, 19288.
[17] a) J. Guan, S. E. Dorris, U. Balachandran, M. Liu, *J. Electrochem. Soc.* **1998**, *145*, 1780; b) C. Zhang, H. Zhao, *Mater. Res. Bull.* **2010**, *45*, 1659.
[18] a) K. S. Knight, *Solid State Ion.* **1994**, *74*, 109; b) S. Yamanaka, M. Fujikane, T. Hamaguchi, H. Muta, T. Oyama, T. Matsuda, S.-I. Kobayashi, K. Kurosaki, *J. Alloys Compd.* **2003**, *359*, 109.
[19] Z. Shao, W. Zhou, Z. Zhu, *Prog. Mater. Sci.* **2012**, *57*, 804.
[20] W. C. Chueh, C. Falter, M. Abbott, D. Scipio, P. Furler, S. M. Haile, A. Steinfeld, *Science* **2010**, *330*, 1797.
[21] D. Vignesh, B. K. Sonu, E. Rout, *Energy Fuels* **2022**, *36*, 7219.
[22] S. Nikodemski, J. Tong, R. O'Hayre, *Solid State Ion.* **2013**, *253*, 201.

[23] J. Yuan, J. Sun, J. Wang, H. Zhang, S. Dong, J. Jiang, L. Deng, X. Zhou, X. Cao, *J. Alloys Compd.* **2018**, *740*, 519.
[24] X. Xu, Y. Chen, W. Zhou, Z. Zhu, C. Su, M. Liu, Z. Shao, *Adv. Mater.* **2016**, *28*, 6442.
[25] J. Wu, R. A. Davies, M. S. Islam, S. M. Haile, *Chem. Mater.* **2005**, *17*, 846.
[26] C. Gionco, M. C. Paganini, E. Giamello, R. Burgess, C. Di Valentin, G. Pacchioni, *Chem. Mater.* **2013**, *25*, 2243.
[27] F. J. A. Loureiro, N. Nasani, G. S. Reddy, N. R. Munirathnam, D. P. Fagg, *J. Power Sources* **2019**, *438*, 226991.
[28] J. R. Groza, R. J. Dowding, *Nanostruct. Mater.* **1996**, *7*, 749.
[29] A. L. Maximenko, E. A. Olevsky, *Acta Mater.* **2004**, *52*, 2953.
[30] X. Guo, H. Xu, W. Li, Y. Liu, Y. Shi, Q. Li, H. Pang, *Adv. Sci.* **2023**, *10*, 2206084.
[31] D. Guan, J. Zhong, H. Xu, Y.-C. Huang, Z. Hu, B. Chen, Y. Zhang, M. Ni, X. Xu, W. Zhou, Z. Shao, *Appl. Phys. Rev.* **2022**, *9*, 011422.
[32] X. Hu, J. Chen, W. Qu, R. Liu, D. Xu, Z. Ma, X. Tang, *Environ. Sci. Technol.* **2021**, *55*, 5435.
[33] D.-C. Sergentu, C. H. Booth, J. Autschbach, *Chem.-Eur. J.* **2021**, *27*, 7239.
[34] D. Neagu, G. Tsekouras, D. N. Miller, H. Ménard, J. T. S. Irvine, *Nat. Chem.* **2013**, *5*, 916.
[35] a) P.-L. Chen, I. W. Chen, *J. Am. Ceram. Soc.* **1997**, *80*, 637; b) J. Zheng, J. S. Reed, *J. Am. Ceram. Soc.* **1989**, *72*, 810; c) I. Arvanitidis, D. Siche, S. Seetharaman, *Metall. Mater. Trans. B* **1996**, *27*, 409.
[36] P. E. Blöchl, *Phys. Rev. B* **1994**, *50*, 17953.
[37] M. Ernzerhof, G. E. Scuseria, *J. Chem. Phys.* **1999**, *110*, 5029.
[38] a) S. Grimme, J. Antony, S. Ehrlich, H. Krieg, *J. Chem. Phys.* **2010**, *132*, 154104; b) D. Guan, H. Xu, Q. Zhang, Y. C. Huang, C. Shi, Y. C. Chang, X. Xu, J. Tang, Y. Gu, C. W. Pao, S. C. Haw, J. M. Chen, Z. Hu, M. Ni, Z. Shao, *Adv. Mater.* **2023**, *35*, 2305074.
[39] a) W. Li, H. Xu, H. Zhang, F. Wei, L. Huang, S. Ke, J. Fu, C. Jing, J. Cheng, S. Liu, *Nat. Commun.* **2023**, *14*, 5235; b) Z. Lv, H. Xu, W. Xu, B. Peng, C. Zhao, M. Xie, X. Lv, Y. Gao, K. Hu, Y. Fang, W. Dong, F. Huang, *Adv. Energy Mater.* **2023**, *13*, 2300790.
[40] W. Xiao, K. Yoo, J. H. Kim, H. Xu, *Adv. Sci.* **2023**, 2303916.
[41] W. Xiao, G. K. Kiran, K. Yoo, J. H. Kim, H. Xu, *Small* **2023**, *19*, 2206750.
[42] H. Xu, J. Z. Zhu, C. Zou, F. Zhang, D. Ming, D. Guan, L. Ma, *Energy Fuels* **2023**, *37*, 16781.
[43] a) H. Xu, D. Guan, *ACS Appl. Mater. Interfaces* **2022**, *14*, 51190; b) H. Xu, D. Guan, L. Ma, *Nanoscale* **2023**, *15*, 2756.